npj Climate and Atmospheric Science https://doi.org/10.1038/s41612-026-01372-1

Article in Press

Asymmetric response of day-to-day temperature variability to CO_2 forcing over Northern Hemisphere mid–high latitudes

Received: 3 November 2025

Accepted: 25 February 2026

Cite this article as: Gan, R., Hu, K., Liu, Q. *et al.* Asymmetric response of day-to-day temperature variability to CO_2 forcing over Northern Hemisphere mid–high latitudes. *npj Clim Atmos Sci* (2026). https://doi.org/10.1038/s41612-026-01372-1

Ruyu Gan, Kaiming Hu, Qi Liu, Gang Huang & Suqin Zhang

Asymmetric Response of Day-to-Day Temperature Variability to CO_2 forcing over Northern Hemisphere Mid–High Latitudes

Ruyu Gan[1,2], Kaiming Hu[3*], Qi Liu[4*], Gang Huang[2,5], Suqin Zhang[6,7]

[1]*Ocean College, Jiangsu University of Science and Technology, Zhenjiang, China*

[2]*Key Laboratory of Earth System Numerical Modeling and Application, Institute of Atmospheric Physics, Chinese Academy of Sciences, Beijing, China*

[3]*College of Resource Environment and Tourism, Capital Normal University, Beijing, 100048, China.*

[4]*School of Atmospheric Sciences, Nanjing University, Nanjing 210023, China*

[5]*University of Chinese Academy of Sciences, Beijing 100049, China*

[6]*Faculty of Geography, Yunnan Normal University, Kunming, China*

[7]*Key Laboratory of Meteorological Disaster (KLME), Ministry of Education & Collaborative Innovation Center on Forecast and Evaluation of Meteorological Disasters(CIC-FEMD), Nanjing University of Information Science & Technology*

*Corresponding author:

Kaming Hu (hkm@mail.iap.ac.cn) and Qi Liu (qiliu@nju.edu.cn)

***Corresponding authors: Kaiming Hu and Qi Liu**

(Kaiming Hu) College of Resource Environment and Tourism, Capital NormalUniversity, Bejing, 100048, China. E-mail: hkm@mail.iap.ac.cn

(Qi Liu) School of Atmospheric Sciences, Nanjing University, Nanjing, China. E-mail: qiliu@nju.edu.cn

Abstract

Day-to-day temperature variability (DTDT) quantifies short-term temperature fluctuations and indicates weather-scale variability. Using idealized carbon dioxide removal (CDR) experiments, we assess the response asymmetry of DTDT over Northern Hemisphere mid-to-high latitudes under symmetric CO_2 ramp-up (RU) and ramp-down (RD) pathways. DTDT decreases with increasing CO_2 and remains strongly suppressed for about two decades after the CO_2 peak. Comparing CO_2 RU and RD periods with identical CO_2 concentrations, DTDT is systematically weaker during RD than during RU, indicating a pronounced response asymmetry to CO_2 forcing. This asymmetry is strongest in boreal winter and weaker in boreal summer. Using a decomposition of the thermodynamic energy equation, we find that the response asymmetry is primarily associated with weakened near-surface horizontal temperature advection, with additional contribution from changes in the variability of net surface radiative forcing. These results highlight the necessity of considering asymmetric and delayed recovery of short-term temperature variability in climate mitigation.

Introduction

Day-to-day temperature variability (DTDT) represents rapid weather-scale fluctuations that exert substantial impacts on public health, ecosystem stability, and socioeconomic activities[1-5]. Increased DTDT has been linked to more frequent temperature-related extremes[2,3], elevated risks of heat- or cold-related morbidity and mortality[4,6,7], reduced crop yields[8], and suppressed economic growth in low-latitude regions[9]. Recent evidence suggests that extreme day-to-day temperature changes represent a distinct category of weather extremes and, in many regions, impose stronger human-health impacts than diurnal temperature range[5].

In recent years, abrupt DTDT transitions have occurred frequently worldwide, causing substantial socioeconomic and ecological impacts[5,10-13]. For example, in September 2020, temperatures across the Rocky Mountains in North America plummeted by over 20 °C within 24 hours, leading to widespread power outages and property losses[14]. In March 2025, southern China experienced an abrupt temperature fluctuation of nearly 30 °C within two days, with daily maxima first rising and then dropping sharply. Such extreme variability can severely damage crops that bloom prematurely during false spring conditions[15,16]. Observational evidence shows widespread declines in DTDT over the 20th century across regions such as North America, northern Europe, and China[17-19], though the magnitude and sign of changes vary seasonally and regionally. Multi-model simulations further suggest a continued decline in DTDT over the Northern Hemisphere mid–high latitudes under both warming[17,19] and low-emission pathways[20]. These changes have been closely linked to Arctic amplification[21] and storm-track activity[22].

Since the Industrial Revolution, anthropogenic emissions of greenhouse gases, particularly carbon dioxide (CO_2), have driven sustained global warming and profoundly altered the Earth's climate system[23-27]. To mitigate climate risks, the Paris Agreement aims to limit global warming to below 2°C and pursue efforts toward 1.5°C above preindustrial levels[28,29]. Achieving this target requires not only deep carbon emission cuts but also the deployment of carbon dioxide removal (CDR) technologies to reduce atmospheric CO_2 concentrations[30-32]. Owing to the ocean's large heat capacity, substantial heat is absorbed during the CO_2 ramp-up (RU) phase; during the ramp-down (RD) phase, this stored heat is gradually released through slow oceanic adjustment processes[33], exerting influences on global climate and potentially delaying climate recovery in some regions[34,35]. Idealized CDR experiments have been widely used to assess the response asymmetry and hysteresis of the climate system[36-41]. Results show that

even after CO_2 concentrations return to their initial levels, many components of the climate system, including global temperature and precipitation[42-46], sea level[47], the Antarctic ice sheet[48-50], the Arctic sea-ice[51-53], the position of the intertropical convergence zone[54], and the Atlantic Meridional Overturning Circulation[55] all exhibit different level of hysteresis in their recovery. Regionally, hysteresis features have also been identified in tropical Pacific SST[56], East and South Asian precipitation[57,58], and ENSO-related circulation responses[59-63].

Despite these advances, the behavior of DTDT under CDR scenarios remains poorly understood. In particular, it is unclear whether DTDT exhibits asymmetric responses between the RU and RD phases under equal CO_2 concentrations, and what are the mechanisms governing these changes. Here, we utilize daily outputs from six models participating in Phase 6 of the Coupled Model Intercomparison Project (CMIP6)[64] under idealized CO_2 ramp-up and ramp-down experiments to examine the asymmetric response of DTDT over the Northern Hemisphere mid–high latitudes. These experiments include the 1pctCO_2 simulation from CMIP6, in which atmospheric CO_2 concentrations increase at 1% per year from pre-industrial levels, and the corresponding 1pctCO_2-cdr simulation from the Carbon Dioxide Removal Model Intercomparison Project (CDRMIP)[30], in which CO_2 concentrations are subsequently reduced at the same rate. We further explore the mechanisms underlying the asymmetric DTDT response using diagnostics based on the near-surface thermodynamic energy equation.

Result

Asymmetric response of daily temperature variability in the Northern Hemisphere mid–high latitudes

Daily temperature variability is quantified using the day-to-day temperature change index, defined as the mean absolute difference in near-surface daily mean 2-m temperature between consecutive days over a given period (see “Methods” section). To assess whether DTDT in the Northern Hemisphere (NH) mid–high latitudes exhibits an asymmetric response under CDR scenarios, we define the CO_2 RD period as years 250–279 and select the RU period as years 1–30, when the atmospheric CO_2 concentrations are equivalent to those during the RD period.

Figure 1 shows the annual-mean DTDT anomalies relative to the preindustrial (PI) baseline during the RU and RD periods. Multimodel ensemble results indicate a marked weakening of DTDT across NH

mid–high latitudes during the RU period (Fig. 1a), consistent with patterns under global-warming scenarios[16]. In contrast, the reduction in DTDT becomes more pronounced during the RD period relative to PI (Fig. 1b). For example, during the ramp-down (RD) period, the annual-mean DTDT decreases by approximately 0.30 °C over Eurasia and 0.22 °C over North America, corresponding to reductions of about 11% and 8% relative to their respective pre-industrial (PI) climatological means (2.69 °C and 2.68 °C; Figs. S1 and S2a). In contrast, during the ramp-up (RU) period, the corresponding decreases are much smaller, amounting to only 0.09 °C (3% relative to PI) over Eurasia and 0.06 °C (2% relative to PI) over North America, respectively. Thus, despite identical CO_2 concentrations, the reduction in DTDT during RD is evidently stronger than that during RU (Fig. 1c). Extending the comparison window to 50 years yields consistent results (Fig. S3), confirming the robustness of this asymmetric response under CDR conditions. Individual-model results (Fig. S4) also demonstrate that all six models simulate stronger DTDT reductions during RD than during RU.

To further test the robustness of this asymmetric behavior, we analyze the temporal evolution of the regional-mean DTDT over the Northern Hemisphere mid–high latitudes (50°–75°N, 0°–360°E) alongside the corresponding CO_2 concentrations throughout the entire ramp-up and ramp-down phases. Figure 1d presents the regional-mean DTDT response to changing CO_2 concentrations. The ensemble-mean DTDT differs systematically between ramp-up and ramp-down at equal CO_2 concentrations. DTDT decreases with increasing CO_2 and remains its maximum reduction for approximately two decades after CO_2 concentrations peak. The magnitude of DTDT reduction is consistently larger during RD than during RU. When expressed as percentage changes relative to the PI climatological mean, DTDT is reduced by nearly 20% around the time of peak CO_2 and then relaxes gradually, remaining suppressed by ~6–10% during the RD phase (Fig. S5a). Although internal variability introduces some inter-model differences, all six models reproduce the ensemble-mean features of both delayed and asymmetric responses (Fig. S6). Under equivalent CO_2 concentrations, DTDT generally decreases more during the CO2 RD phase than during the CO2 RU phase, confirming that day-to-day temperature variability exhibits asymmetry under CO_2 removal.

Beyond annual means, seasonal analyses of the asymmetric DTDT response reveal clear seasonal contrasts, with a much weaker response in summer compared to other seasons (Fig. 2; Figs. S7 and S8).

In absolute terms, the reduction during the RD phase relative to the RU phase is largest in winter (−0.24 °C; Fig. 2d), followed by autumn (−0.20 °C; Fig. 2c) and spring (−0.19 °C; Fig. 2a), with a much weaker response in summer (−0.05 °C; Fig. 2b). Notably, localized DTDT increases occur along northern Eurasian high latitudes regions in boreal summer (Fig. 2b).

When expressed relative to the PI climatology, DTDT decreases during the RD phase by −8.7 % ± 1.9 % ("±" denotes the 1.0 standard deviation bootstrap uncertainty of the multi-model mean based on 10,000 resamples) for the annual mean, −9.6 % ± 2.1 % in MAM, −3.8 % ± 1.2 % in JJA, −10.4 % ± 2.7 % in SON, and −9.1 % ± 1.4 % in DJF (Fig. S5f). In contrast, the corresponding reductions during the RU phase are substantially smaller, amounting to −2.5 % ± 0.7 % annually and remaining below −3 % in all seasons (Fig. S5f). As a result, the differential response between the RD and RU phases (RD–RU), normalized by the PI climatology, reaches −6.2 % ± 1.8 % for the annual mean, with the strongest contrasts in autumn (−7.6 % ± 2.4 %), spring (−7.3 % ± 2.2 %), and winter (−6.1 % ± 1.4 %), while the response in summer remains much weaker (−2.6 % ± 1.1 %). These results show that DTDT is systematically more strongly reduced during the ramp-down phase than during the ramp-up phase under equal CO_2 concentrations, even when changes are expressed relative to the PI baseline.

Daily temperature variability in Northern Hemisphere mid–high latitudes is significantly weakened under CO_2 removal, with a larger reduction during the ramp-down period than during ramp-up. We additionally computed DTDT using daily maximum and minimum temperatures, and the results that are consistent with those based on daily-mean temperature (Figs. S9 and S10). This asymmetric response implies a delayed recovery of rapid weather fluctuations even when atmospheric CO_2 concentrations return to preindustrial levels.

Asymmetric response of rapid temperature variation events

Given the robustness of the asymmetric DTDT response, a natural question arises: in which range of temperature fluctuations do these changes primarily occur? To address this question, Figure 3 presents the frequency distributions of the absolute day-to-day temperature difference ($|\delta T|$) during the CO_2 RU and RD phases over NH mid–high latitudes (50°N-75°N,0°-360°E). On the annual scale (Fig. 3a), the frequency of weak temperature fluctuations ($|\delta T| < 1$ °C) increases during the RD phase compared with

the RU phase, whereas the frequency of strong fluctuations (|δT|> 2 °C) decreases markedly. This pattern indicates that CO_2 removal shifts the distribution of temperature fluctuations toward smaller amplitudes, reflecting a substantial reduction in the occurrence of strong rapid temperature variation events during the ramp-down phase compared with the ramp-up phase.

At the seasonal scale, this asymmetric behavior persists across most seasons but with varying magnitudes across temperature ranges. In boreal winter, the frequency of moderate-to-strong fluctuations (|δT| = 2–5°C) decreases substantially during the CO_2 ramp-down phase, particularly within the 2–3°C and 3–4 °C intervals (Fig. 3b). Boreal spring exhibits a similar reduction across 2–4°C range (Fig. 3c), while in boreal autumn, the reductions are most evident for moderate fluctuations of 1–3 °C (Fig. 3e). These consistent decreases across mid-to-high temperature ranges indicate a systematic suppression of moderate-to-strong day-to-day variability during CO_2 decline. In contrast, the boreal summer response is less pronounced, with little change in the most frequent weak-transition bin (0–1°C) and only small differences elsewhere (Fig. 3d). This result suggests that large-amplitude rapid temperature fluctuations weaken more strongly during the CO_2 ramp-down period, leading to fewer extreme rapid warming or cooling events.

Mechanisms underlying the asymmetric response of DTDT

The above results demonstrate that despite identical CO_2 concentrations, the day-to-day temperature variability over the NH mid–high latitudes exhibit a pronounced asymmetric change between the RU and RD phases. This raises an important question: which physical processes control this asymmetric response? To answer this question, we diagnose the sources of DTDT changes using a near-surface thermodynamic energy equation (see "Methods" section). Within this framework, RD–RU differences in DTDT are primarily associated with changes in near-surface horizontal temperature advection (ΔTADV) and with changes in the day-to-day variability of near-surface net radiative forcing (ΔDTDNRF).

Figure 4a–e presents the spatial distribution of RD–RU differences in near-surface horizontal temperature advection for the annual mean and four seasons. Because daily 10 m winds required to compute TADV are available for only four models (CanESM5, CNRM-ESM2-1, MIROC-ES2L and GFDL-ESM4), the analysis is based on their multimodel mean. Across Northern Hemisphere mid–high

latitudes, ΔTADV exhibits a widespread weakening in the annual mean and in all seasons, with the largest reductions over high-latitude North America and Eurasia. These regions closely coincide with those exhibiting the strongest DTDT reductions.

Seasonal patterns further highlight this correspondence. In spring, the most pronounced weakening of ΔTADV occurs over northern Eurasia, matching the region of strongest springtime DTDT reduction (Fig. 4b versus Fig. 2a). In autumn and winter, the largest ΔTADV reductions are concentrated over high-latitude North America, coinciding with marked DTDT weakening (Fig. 4d, 4e versus Fig. 2c, 4d). By contrast, summer ΔTADV weakening is substantially smaller (Fig. 4c), consistent with the relatively modest summer DTDT changes. A localized summer enhancement of ΔTADV over northern Canada aligns with a slight local increase in summer DTDT, indicating that regional advection changes can modulate summertime variability.

A reduction in TADV reflects a weaker contribution of warm and cold air advection to near-surface temperature fluctuations, thereby suppressing short-term temperature variability. Such a systematic weakening is consistent with a more stable large-scale circulation and reduced synoptic activity, conditions that are less conducive to rapid temperature fluctuations[65].

We further decompose ΔTADV into its zonal and meridional components (Fig. S11 and Fig. 4f–j). Both components exhibit a widespread weakening across Northern Hemisphere mid–high latitudes. However, the meridional component (Fig. 4f–j) shows spatial patterns and amplitudes that are more consistent with those of total horizontal temperature advection (Fig. 4a–e) across seasons than the zonal component (Fig. S11). In particular, during spring, autumn, and winter, ΔTADVy reproduces the main regional features of ΔTADV, including the pronounced reductions over high-latitude North America and Eurasia. This meridional dominance is consistent with a concurrent weakening of day-to-day variability in near-surface meridional wind (ΔDTDvas; Fig. S12f–j) and with a reduced meridional temperature gradient over broad regions (Fig. S13), both of which act to suppress meridional thermal advection. These results suggest that changes in meridional warm and cold air advection play a leading role in the diagnosed weakening of near-surface horizontal temperature advection, thereby contributing to the suppression of day-to-day temperature variability. Individual-model results indicate that the weakening of ΔTADV and

its seasonal dependence are broadly consistent across the four models, with differences mainly in regional amplitude (Figs. S14 and S15).

In addition to dynamical processes, diabatic processes can modulate DTDT through changes in the day-to-day variability of net surface radiative forcing (ΔDTDNRF). Here ΔDTDNRF is used as a qualitative diagnostic of radiative modulation rather than a quantitative contribution to DTDT, because it is expressed in radiative units. Net radiative forcing integrates surface shortwave and longwave radiation, and its daily variability characterizes the radiative influence on weather-scale temperature fluctuations. Figure 5 shows the spatial distribution of ΔDTDNRF based on the multimodel mean of three models (CanESM5, CNRM-ESM2-1 and MIROC-ES2L), with stippling indicating agreement on the sign of change. Model-by-model diagnostics show that the sign and large-scale structure of ΔDTDNRF are generally consistent across the three models (Fig. S16).

In the annual mean and spring, ΔDTDNRF is weakly positive across much of Northern Hemisphere mid to high latitudes, particularly over North America and northern Eurasia (Fig. 5a, b). These anomalies slightly offset the DTDT reduction associated with weakened horizontal temperature advection, although dynamical changes dominate in most regions. In summer, ΔDTDNRF displays positive anomalies over high-latitude North America and northern Eurasia, while negative anomalies prevail over mid-latitude Eurasia (Fig. 5c). This spatial contrast is consistent with the weak summer enhancement of DTDT over northern Eurasia, indicating a seasonally dependent radiative modulation superimposed on the dynamical background. In autumn (Fig. 5d), ΔDTDNRF exhibits weak positive anomalies over North America but widespread negative anomalies over Eurasia, implying partial offsetting over the North America and reinforcement of DTDT weakening in the Eurasia. In winter (Fig. 5e), negative ΔDTDNRF over northern Eurasia co-occurs with strongly negative ΔTADV, such that both effects act in the same direction and contribute to the pronounced wintertime DTDT reduction.

Decomposing net radiation into net shortwave and net longwave components shows that ΔDTDNSWR and ΔDTDNLWR share similar large-scale structures in most seasons (Fig. 5f–j and Fig. 5k–o; Figs. S17 and S18). In summer, however, northern high-latitude Eurasia shows a pronounced positive ΔDTDNSWR (Fig. 5h) without a comparable ΔDTDNLWR signal (Fig. 5m). The local positive ΔDTDNRF (Fig. 5c) therefore mainly reflects enhanced shortwave variability. This co-occurs with the

weak local summer increase in DTDT, providing a physically consistent interpretation for the regional signal.

Regional variability can be influenced by land–atmosphere coupling via its regulation of surface energy and moisture exchanges[66-68]. Land-surface states therefore provide physically interpretable constraints on the spatial pattern of diabatic variability. Large parts of Northern Hemisphere mid- to high-latitude land are drier in RD than in RU, with negative anomalies in mean soil moisture over high-latitude Eurasia and much of North America (Δmean mrsos; Fig. S19k–o). Day-to-day variability in near-surface relative humidity weakens and co-varies spatially with reduced cloud variability (ΔDTDhurs and ΔDTDclt; Fig. S19a–j). Regions of negative ΔDTDclt co-locate with weaker variability in both downward and upward longwave radiation (ΔDTDrlds and ΔDTDrlus; Fig. S20), and align with predominantly negative anomalies in net longwave variability (ΔDTDNLWR; Fig. 5k–o). This moisture–cloud–longwave co-variation is consistent with established land–atmosphere coupling pathways in which soil moisture deficits alter surface flux partitioning and boundary-layer moistening, thereby modulating radiative and thermodynamic variability on weather timescales[68-70]. Consistent with this context, day-to-day turbulent flux variability reorganizes under RD, with enhanced sensible heat flux variability over North America and parts of Eurasia and increased latent heat flux variability across much of mid- to high-latitude land (ΔDTDhfss and ΔDTDhfls; Fig. S21). These co-variations are not treated as independent predictors of ΔDTDT, but as process-consistent context for the spatial structure of the diabatic terms. The diagnostic decomposition nevertheless indicates that the dominant contribution to the DTDT asymmetry remains the systematic weakening of near-surface horizontal temperature advection.

Discussion

Using idealized CO_2 ramp-up and ramp-down experiments from six CMIP6 models, we identify a pronounced asymmetry in Northern Hemisphere mid–high-latitude day-to-day temperature variability under a symmetric CO_2 pathway. For periods with identical atmospheric CO_2 concentrations, DTDT is systematically weaker during ramp-down than during ramp-up, indicating an asymmetric response of weather-scale temperature fluctuations under CO_2 removal. This asymmetry is seasonally structured, with the strongest signal in winter and weaker, more localized responses in summer.

The diagnosed DTDT asymmetry is dominated by a weakening of near-surface horizontal temperature advection, with the meridional component contributing most to the spatial structure. This suggests a reduced day-to-day exchange of warm and cold air masses over northern land during ramp-down, even at identical CO_2 concentrations. Superimposed on this dynamical background, diabatic processes exhibit coherent covariation with land-surface and cloud-related changes: mid–high-latitude land tends to be drier, boundary-layer humidity and cloud variability weaken, and longwave radiative variability is reduced over similar regions. These patterns are consistent with established land–atmosphere coupling pathways in which soil moisture influences surface flux partitioning and boundary-layer moistening, thereby modulating radiative and thermodynamic variability on weather timescales. In summer, enhanced shortwave radiative variability over northern Eurasia coincides with weak local DTDT increases, suggesting a seasonally dependent radiative modulation that does not overturn the dominant dynamical control. Previous studies suggest that Northern Hemisphere mid–high-latitude DTDT is closely tied to synoptic advection and large-scale temperature gradients[4,5,17]. Arctic amplification weakens the meridional temperature gradient, which can damp synoptic variability and reduce horizontal thermal advection, consistent with a decline in DTDT that strengthens under higher-emission scenarios. Quantifying how these gradient and circulation adjustments translate into DTDT changes, and how they interact with CO_2-removal pathways, remains an open question.

A weakening of subseasonal and synoptic temperature variability over Northern Hemisphere high latitudes in association with Arctic amplification has been widely discussed[17,21,70]. Our work adds to this line of research by highlighting an additional dimension related to CO_2 removal pathways. A reduction in high-latitude day-to-day temperature variability may also carry broad implications. When superimposed on the background warming trend, weaker short-term variability may be associated with longer-lived warm anomalies and longer heatwave-like episodes. Meanwhile, milder winters can enhance the overwinter survival of pests and pathogens (for example, forest insects and disease agents), with potential consequences for agricultural production and forest health. Reduced short-term variability may further increase ecosystem adaptation risks, for instance by altering phenological synchrony and affecting biodiversity. Because the day-to-day temperature variability response is asymmetric, it should be explicitly considered in future impact assessments and adaptation strategies, including targeted

adjustments in agricultural management, energy planning, and public health preparedness to help reduce potential adverse impacts.

Our analysis is based on a limited set of CMIP6 models rather than a single-model large ensemble, which may constrain our ability to robustly disentangle forced changes from internal variability in the diagnosed DTDT asymmetry. Recent studies have addressed CO_2 removal pathways using CO_2 ramp-up and ramp-down experiments with the 28-member CESM large ensemble to examine hysteresis and irreversibility, for example, responses in surface temperature and precipitation[43] and ENSO-related characteristics[59,62,63]. Extending the present analysis to a large-ensemble framework would help constrain uncertainty and test the robustness of DTDT responses against internal variability. In addition, recent studies suggest that under continued warming, extreme day-to-day temperature transitions may intensify across many mid- to low-latitude regions[5] where the historical evolution and dominant controls of day-to-day variability differ from those in Northern Hemisphere mid–high latitudes[5,17]. Whether comparable RU–RD asymmetry emerges in these regions under equal CO_2 conditions, and which processes govern such a response, warrants targeted investigation.

Methods

CMIP6 experiments and data processing

We used daily outputs from the 1pctCO_2, 1pctCO_2-cdr and piControl experiments of the CMIP6[64]. In the 1pctCO_2 experiment, atmospheric CO_2 concentrations increase by approximately 1 % yr^{-1} from the pre-industrial level (≈ 285 ppm) and reach four times that level by year 140. Starting from this state, the 1pctCO_2-cdr experiment applies a symmetric decrease in CO_2 at the same rate over the subsequent 140 years, after which concentrations remain fixed at the pre-industrial level for at least 60 years. The

piControl experiment, with CO_2 concentrations held constant at 284.7 ppm, represents a near-equilibrium pre-industrial climate state.

We merge years 1–139 of the 1pctCO_2 experiment with years 1–140 of the 1pctCO_2-cdr experiment to construct a complete RU–RD CO_2 pathway (Fig. 1d). The climatology of the final 100 years of piControl is used as the pre-industrial reference (PI). Six CMIP6 models are used in this analysis: ACCESS-ESM1-5, CanESM5, CNRM-ESM2-1, GFDL-ESM4, MIROC-ES2L and UKESM1-0-LL. Daily near-surface daily-mean temperature at 2m is used to calculate day-to-day (DTD) temperature variability. Model outputs are bilinearly interpolated onto a 1° × 1° grid, and averaged to form the multi-model ensemble mean (MME). The primary DTDT analysis based on daily-mean temperature at 2m is performed for all six models. Mechanistic diagnostics use reduced model subsets due to data availability: horizontal temperature advection (ΔTADV) is computed for the four models with daily 10-m winds (CanESM5, CNRM-ESM2-1, GFDL-ESM4, MIROC-ES2L), and radiative-variability diagnostics (ΔDTDNRF and its shortwave/longwave components) are computed for the three models with complete daily surface radiative flux components (CanESM5, CNRM-ESM2-1, MIROC-ES2L).

Definition of rapid temperature variability

In this study, we quantify rapid temperature fluctuations on the weather timescale using a simplified metric of DTDT. At each grid point, DTDT is defined as the absolute difference in near-surface daily-mean air temperature at 2 m between two consecutive days, following previous studies[18,72,73].

$$\mathrm{DTDT} = \frac{1}{n-1}\sum_{i=1}^{n-1}|T_{i+1} - T_i| \quad (1)$$

where T_i is the daily-mean 2-m air temperature on day i, and n is the total number of days within the analyzed period.

This diagnostic has been widely applied to assess high-frequency climate variability and its response to external forcing[1,4,5,17,19,20,74]. To assess the robustness of the diagnosed DTDT responses, we additionally compute day-to-day variability based on daily maximum and minimum temperatures (tasmax and tasmin). The resulting spatial patterns are highly consistent with those obtained from daily-mean

temperature, indicating that the main conclusions are insensitive to the specific temperature metric employed (Figs. S9 and S10).

Day-to-day variability of surface energy balance and circulation variables

To diagnose the physical processes associated with changes in DTDT, we further compute the day-to-day variability of a suite of surface energy balance and circulation variables. For a given variable X, its day-to-day variability is defined analogously as

$$\mathrm{DTD}x = \frac{1}{n-1}\sum_{i=1}^{n-1}|X_{i+1} - X_i| \tag{2}$$

Using this definition, we compute annual and seasonal-mean variability for boreal winter (DJF), spring (MAM), summer (JJA) and autumn (SON). The diagnostics cover key components of the surface energy and moisture budget, including shortwave and longwave radiative fluxes, turbulent sensible and latent heat fluxes, total cloud fraction, near-surface horizontal winds, and surface soil moisture. Specifically, we analyze downward and upward shortwave radiation (rsds and rsus), downward and upward longwave radiation (rlds and rlus), sensible and latent heat fluxes (hfss and hfls), total cloud fraction (clt), 10-m zonal and meridional winds (uas and vas), and total column soil moisture (mrsos).

Diagnostic decomposition of DTDT changes based on the thermodynamic energy equation

To quantitatively identify the physical mechanisms driving changes in DTDT, we apply a diagnostic decomposition framework based on the near-surface thermodynamic energy equation. According to the near-surface thermodynamic energy equation[75], the daily mean temperature tendency between two consecutive days can be expressed as

$$\delta T = \frac{\partial T}{\partial t} = -\mathrm{V}\cdot\nabla T + \left(\frac{RT}{c_p P} - \frac{\partial T}{\partial P}\right)\omega + \frac{1}{c_p}\frac{\partial Q}{\partial t} \tag{3}$$

Where T denotes the daily mean near-surface air temperature at 2 m (°C), and V is the daily mean horizontal wind vector at 10 m (m s^{-1}). ∇ represent the horizontal temperature gradient operator. R is the gas constant for dry air (287 $J\cdot K^{-1}\cdot kg^{-1}$), $c_p$is the specific heat capacity of dry air at constant pressure

(1004 $J \cdot K^{-1} \cdot kg^{-1}$), and P denotes atmospheric pressure (Pa). The variable ω represents the near-surface vertical velocity in pressure coordinates ($Pa \cdot s^{-1}$), and Q is the daily diabatic heating ($J \cdot kg^{-1}$).

Following previous studies[1,20], DTDT can be related to the thermodynamic energy equation by combining Eqs. (1) and (3), such that DTDT is expressed as the time mean of the absolute daily temperature tendency:

$$\mathrm{DTDT} = \frac{1}{n-1}\sum_{i=1}^{n-1}|\delta T_i| = \frac{1}{n-1}\sum_{i=1}^{n-1}\left|\frac{\partial T}{\partial t_i}\right| \tag{4}$$

Based on Eq. (3), DTDT can be diagnostically decomposed into contributions from horizontal temperature advection, adiabatic processes associated with vertical motion, and diabatic heating:

$$\mathrm{term1} = \frac{1}{n-1}\sum_{i=1}^{n-1}|-V_i \cdot \nabla T_i| \tag{5}$$

$$\mathrm{term2} = \frac{1}{n-1}\sum_{i=1}^{n-1}\left|\left(\frac{RT_i}{c_p P_i} - \frac{\partial T}{\partial P_i}\right)\omega_i\right| \tag{6}$$

$$\mathrm{term3} = \frac{1}{n-1}\sum_{i=1}^{n-1}\left|\frac{1}{c_p}\frac{\partial Q}{\partial t}\right| \tag{7}$$

Accordingly, changes in DTDT between the CO_2 ramp-down (RD) and ramp-up (RU) periods can be diagnostically expressed as

$$\Delta\mathrm{DTDT} \approx \Delta\mathrm{term1} + \Delta\mathrm{term2} + \Delta\mathrm{term3} \tag{8}$$

where Δ denotes the difference between the RD period and the RU period. Here, $\Delta\mathrm{term1}$ represents changes in daily mean near-surface horizontal temperature advection, $\Delta\mathrm{term2}$ denotes changes in adiabatic compression or expansion associated with vertical motion, and $\Delta\mathrm{term3}$ accounts for changes in diabatic heating.

At near-surface levels, $\Delta\mathrm{term2}$ is generally small compared to the other terms and is therefore neglected in the analysis of long-term DTDT changes[76]. To further characterize the circulation-related contribution, $\Delta\mathrm{term1}$ is separated into zonal and meridional components, allowing an assessment of the relative roles of different flow directions:

$$\Delta\mathrm{term1} = \Delta\left(\frac{1}{n-1}\sum_{i=1}^{n-1}|-V \cdot \nabla T|\right) \approx \Delta\left(\frac{1}{n-1}\sum_{i=1}^{n-1}\left|-u \cdot \frac{\partial T}{\partial \mathrm{x}}\right|\right) + \Delta\left(\frac{1}{n-1}\sum_{i=1}^{n-1}\left|-v \cdot \frac{\partial T}{\partial \mathrm{y}}\right|\right) \tag{9}$$

This formulation is used to diagnose the relative contributions of zonal and meridional thermal advection to asymmetric DTDT responses, rather than implying a strict mathematical decomposition of the total advection term. The horizontal temperature gradient ∇T characterizes the intensity of weather-scale thermal contrasts that interact with near-surface winds to drive temperature advection.

The diabatic term is further characterized using the day-to-day variability of surface net radiation forcing (NRF), which provides a direct measure of radiative adjustments associated with changing greenhouse gas concentrations under carbon dioxide removal. Accordingly, $\Delta\mathrm{term3}$ is approximated as

$$\Delta\mathrm{term3} = \Delta\left(\frac{1}{n-1}\sum_{i=1}^{n-1}\left|\frac{\partial NRF}{\partial t_i}\right|\right) = \Delta\left(\frac{1}{n-1}\sum_{i=1}^{n-1}|NRF_{i+1} - NRF_i|\right) \quad (10)$$

where NRF_i is defined as the sum of net surface shortwave and longwave radiative fluxes on day i. Because $\Delta\mathrm{term3}$ has units of W m^{-2}, which differ from those of DTDT, it is not interpreted as a direct quantitative contribution. Instead, changes in $\Delta\mathrm{term3}$ are used as a qualitative diagnostic indicator of how variations in radiative forcing modulate day-to-day temperature variability.

Data availability

The CMIP6 model data used in this study are freely available from the website, https://esgf-node.llnl.gov/projects/cmip6/.

Acknowledgements

We acknowledge the World Climate Research Program, which coordinated and promoted CMIP6 through its Working Group on Coupled Modelling. We thank Chao Liu for helpful discussions and advice. The work was supported by the National Natural Science Foundation of China (Grant Nos. 42406006, 42141019), and the Joint Open Project of Key Laboratory of Meteorological Disaster, Ministry of Education & Collaborative Innovation Center on Forecast and Evaluation of Meteorological Disasters, NUIST (KLME202503)

Author Contributions

K.H. and Q.L. designed the research, provided comments, and revised the manuscript. R.G. performed the analysis and drafted the manuscript. K.H. and Q.L. helped organize and revise the draft. K.H., Q.L., G.H and S.Z. gave comments and contributed to the discussion of the results. R.G., K.H., Q.L., G.H and S.Z. contributed to scientific interpretations and subsequent revisions.

Competing interests

The authors declare no competing financial or non-financial interests.

References

1. Ge, J. *et al.* Deforestation intensifies daily temperature variability in the northern extratropics. *Nat. Commun.* **13**, 5955 (2022).
2. Katz, R. W. & Brown, B. G. Extreme events in a changing climate: variability is more important than averages. *Clim. Change* **21**, 289-302 (1992).
3. Schär, C. *et al.* The role of increasing temperature variability in European summer heatwaves. *Nature* **427**, 332-336, doi:10.1038/nature02300 (2004).
4. Liu, Q. *et al.* Changing rapid weather variability increases influenza epidemic risk in a warming climate. *Environ. Res. Lett.* **15**, 044004 (2020).
5. Liu, Q., Fu, C., Xu, Z. & Ding, A. Global warming intensifies extreme day-to-day temperature changes in mid–low latitudes. *Nat. Clim. Change* **16**, 69-76, doi:10.1038/s41558-025-02486-9 (2026).
6. Guo, Y. *et al.* A large change in temperature between neighbouring days increases the risk of mortality. *PLoS One* **6**, e16511 (2011).
7. Zhan, Z. *et al.* Temperature change between neighboring days and mortality in United States: a nationwide study. *Sci. Total Environ.* **584**, 1152-1161 (2017).
8. Wheeler, M. & Kiladis, G. N. Convectively Coupled Equatorial Waves: Analysis of Clouds and Temperature in the Wavenumber–Frequency Domain. *J. Atmos. Sci.* **56**, 374-399, doi:https://doi.org/10.1175/1520-0469(1999)056<0374:CCEWAO>2.0.CO;2 (1999).
9. Kotz, M., Wenz, L., Stechemesser, A., Kalkuhl, M. & Levermann, A. Day-to-day temperature variability reduces economic growth. *Nat. Clim. Change* **11**, 319-325, doi:10.1038/s41558-020-00985-5 (2021).
10. Vicedo-Cabrera, A. M. *et al.* Associations of inter-and intraday temperature change with mortality. *American journal of epidemiology* **183**, 286-293 (2016).
11. Laucelli, D., Rajani, B., Kleiner, Y. & Giustolisi, O. Study on relationships between climate-

related covariates and pipe bursts using evolutionary-based modelling. *J. Hydroinf.* **16**, 743-757 (2014).

12. Zou, Y., Wang, Y., Zhang, Y. & Koo, J.-H. Arctic sea ice, Eurasia snow, and extreme winter haze in China. *Sci. Adv.* **3**, e1602751 (2017).

13. Marino, G. P., Kaiser, D. P., Gu, L. & Ricciuto, D. M. Reconstruction of false spring occurrences over the southeastern United States, 1901–2007: an increasing risk of spring freeze damage? *Environ. Res. Lett.* **6**, 024015 (2011).

14. Russell, E. N., Loikith, P. C., Ajibade, I., Done, J. M. & Lower, C. The meteorology and impacts of the September 2020 Western United States extreme weather event. *Weather Clim. Extremes* **43**, 100647 (2024).

15. Peterson, T. C., Stott, P. A. & Herring, S. Explaining extreme events of 2011 from a climate perspective. *Bull. Am. Meteorol. Soc.* **93**, 1041-1067 (2012).

16. Ault, T. *et al.* The false spring of 2012, earliest in North American record. *Eos, Transactions American Geophysical Union* **94**, 181-182 (2013).

17. Xu, Z., Huang, F., Liu, Q. & Fu, C. Global pattern of historical and future changes in rapid temperature variability. *Environ. Res. Lett.* **15**, 124073 (2020).

18. Gough, W. Theoretical considerations of day-to-day temperature variability applied to Toronto and Calgary, Canada data. *Theor. Appl. Climatol.* **94**, 97-105 (2008).

19. Liu, Q., Fu, C. & Xu, Z. Revisiting two indices measuring high-frequency daily variability. *Int. J. Climatol.* **44**, 2792-2807, doi:https://doi.org/10.1002/joc.8481 (2024).

20. Wang, P., Ye, F., Yang, Y., Tang, J. & Liao, H. Mitigated rapid temperature variability in the northern mid-high latitudes under carbon neutrality. *Geophys. Res. Lett.* **52**, e2025GL118040 (2025).

21. Screen, J. A. Arctic amplification decreases temperature variance in northern mid- to high-latitudes. *Nat. Clim. Change* **4**, 577-582, doi:10.1038/nclimate2268 (2014).

22. Xu, G. *et al.* Jet stream controls on European climate and agriculture since 1300 ce. *Nature* **634**, 600-608, doi:10.1038/s41586-024-07985-x (2024).

23. Rahmstorf, S. & Coumou, D. Increase of extreme events in a warming world. *Proceedings of the National Academy of Sciences* **108**, 17905-17909 (2011).

24. Lane, J. E., Kruuk, L. E. B., Charmantier, A., Murie, J. O. & Dobson, F. S. Delayed phenology and reduced fitness associated with climate change in a wild hibernator. *Nature* **489**, 554-557, doi:10.1038/nature11335 (2012).

25. Richardson, A. D. *et al.* Ecosystem warming extends vegetation activity but heightens vulnerability to cold temperatures. *Nature* **560**, 368-371, doi:10.1038/s41586-018-0399-1 (2018).

26. Kotz, M., Lange, S., Wenz, L. & Levermann, A. Constraining the pattern and magnitude of

projected extreme precipitation change in a multimodel ensemble. *J. Clim.* **37**, 97-111 (2024).

27. Yeh, S.-W., Song, S.-Y., Allan, R. P., An, S.-I. & Shin, J. Contrasting response of hydrological cycle over land and ocean to a changing CO2 pathway. *npj Clim. Atmos. Sci.* **4**, 53, doi:10.1038/s41612-021-00206-6 (2021).

28. Peters, G. P. *et al.* The challenge to keep global warming below 2 C. *Nat. Clim. Change* **3**, 4-6 (2013).

29. Sanderson, B. M., O'Neill, B. C. & Tebaldi, C. What would it take to achieve the Paris temperature targets? *Geophys. Res. Lett.* **43**, 7133-7142 (2016).

30. Keller, D. P. *et al.* The carbon dioxide removal model intercomparison project (CDRMIP): rationale and experimental protocol for CMIP6. *Geosci. Model Dev.* **11**, 1133-1160 (2018).

31. Rogelj, J. *et al.* Scenarios towards limiting global mean temperature increase below 1.5 C. *Nat. Clim. Change* **8**, 325-332 (2018).

32. Realmonte, G. *et al.* An inter-model assessment of the role of direct air capture in deep mitigation pathways. *Nat. Commun.* **10**, 3277 (2019).

33. Long, S.-M. *et al.* Effects of Ocean Slow Response under Low Warming Targets. *J. Clim.* **33**, 477-496, doi:https://doi.org/10.1175/JCLI-D-19-0213.1 (2020).

34. Oh, J.-H. *et al.* Emergent climate change patterns originating from deep ocean warming in climate mitigation scenarios. *Nat. Clim. Change* **14**, 260-266, doi:10.1038/s41558-024-01928-0 (2024).

35. Kim, G.-I. et al. Deep ocean warming-induced El Niño changes. Nat. Commun. 15, 6225, doi:10.1038/s41467-024-50663-9 (2024).

36. Wu, P., Ridley, J., Pardaens, A., Levine, R. & Lowe, J. The reversibility of CO2 induced climate change. Clim. Dyn. 45, 745-754 (2015).

37. Cao, L., Bala, G. & Caldeira, K. Why is there a short-term increase in global precipitation in response to diminished CO2 forcing? Geophys. Res. Lett. 38, doi:https://doi.org/10.1029/2011GL046713 (2011).

38. Wu, P., Wood, R., Ridley, J. & Lowe, J. Temporary acceleration of the hydrological cycle in response to a CO2 rampdown. Geophys. Res. Lett. 37 (2010).

39. Oh, J.-H., An, S.-I., Shin, J. & Kug, J.-S. Centennial Memory of the Arctic Ocean for Future Arctic Climate Recovery in Response to a Carbon Dioxide Removal. Earth's Future 10, e2022EF002804, doi:https://doi.org/10.1029/2022EF002804 (2022).

40. An, S.-I. et al. Global Cooling Hiatus Driven by an AMOC Overshoot in a Carbon Dioxide Removal Scenario. Earth's Future 9, e2021EF002165, doi:https://doi.org/10.1029/2021EF002165 (2021).

41. Liu, C. et al. ENSO skewness hysteresis and associated changes in strong El Niño under a CO2 removal scenario. npj Clim. Atmos. Sci. 6, 117, doi:10.1038/s41612-023-00448-6 (2023).

42. Chadwick, R., Wu, P., Good, P. & Andrews, T. Asymmetries in tropical rainfall and circulation patterns in idealised CO2 removal experiments. Clim. Dyn. 40, 295-316 (2013).

43. Kim, S.-K. et al. Widespread irreversible changes in surface temperature and precipitation in response to CO2 forcing. Nat. Clim. Change 12, 834-840 (2022).

44. Song, S.-Y. et al. Climate sensitivity controls global precipitation hysteresis in a changing CO2 pathway. npj Clim. Atmos. Sci. 6, 156 (2023).

45. Zickfeld, K., MacDougall, A. H. & Matthews, H. D. On the proportionality between global temperature change and cumulative CO2 emissions during periods of net negative CO2 emissions. Environ. Res. Lett. 11, 055006 (2016).

46. Tokarska, K. B. & Zickfeld, K. The effectiveness of net negative carbon dioxide emissions in reversing anthropogenic climate change. Environ. Res. Lett. 10, 094013 (2015).

47. Boucher, O. et al. Reversibility in an Earth System model in response to CO2 concentration changes. Environ. Res. Lett. 7, 024013 (2012).

48. Garbe, J., Albrecht, T., Levermann, A., Donges, J. F. & Winkelmann, R. The hysteresis of the Antarctic ice sheet. Nature 585, 538-544 (2020).

49. Li, S., Hu, K., Huang, G. & Zheng, X. T. The reversibility of Antarctic sea ice loss under CO2 removal scenarios. Geophys. Res. Lett. 52, e2025GL116756 (2025).

50. Pollard, D. & DeConto, R. M. Hysteresis in Cenozoic Antarctic ice-sheet variations. Global Planet. Change 45, 9-21 (2005).

51. Yu, H. et al. Incomplete Arctic Sea-Ice Recovery Under CO2 Removal and Its Effects on the Winter Atmospheric Circulation. Geophys. Res. Lett. 52, e2024GL113541, doi:https://doi.org/10.1029/2024GL113541 (2025).

52. Cajada, M. I., Son, S.-W., Hwang, J., Park, H.-S. & An, S.-I. Regionally-Dependent Arctic Sea Ice Recovery to CO2 Removal. Earth's Future 13, e2024EF005597, doi:https://doi.org/10.1029/2024EF005597 (2025).

53. Heo, E.-S., An, S.-I. & Shin, J. Asymmetric Impact of the Tropical Pacific on Summertime Arctic Sea Ice Trends Under Increasing and Decreasing Greenhouse Gases. Geophys. Res. Lett. 52, e2025GL116352, doi:https://doi.org/10.1029/2025GL116352 (2025).

54. Kug, J.-S. et al. Hysteresis of the intertropical convergence zone to CO2 forcing. Nat. Clim. Change 12, 47-53 (2022).

55. An, S.-I., Kim, H.-J. & Kim, S.-K. Rate-Dependent Hysteresis of the Atlantic Meridional Overturning Circulation System and Its Asymmetric Loop. Geophys. Res. Lett. 48, e2020GL090132, doi:https://doi.org/10.1029/2020GL090132 (2021).

56. Zhou, S., Huang, P., Xie, S.-P., Huang, G. & Wang, L. Varying contributions of fast and slow responses cause asymmetric tropical rainfall change between CO2 ramp-up and ramp-down. Sci. Bull. 67, 1702-1711 (2022).

57. Zhang, S., Qu, X., Huang, G. & Hu, P. Asymmetric response of South Asian summer monsoon rainfall in a carbon dioxide removal scenario. npj Clim. Atmos. Sci. 6, 10 (2023).

58. Song, S.-Y. et al. Asymmetrical response of summer rainfall in East Asia to CO2 forcing. Sci. Bull. 67, 213-222 (2022).

59. Liu, C. et al. Hysteresis of the El Niño–southern oscillation to CO2 forcing. Sci. Adv. 9, eadh8442 (2023).

60. Zhang, W. et al. Irreversibility of ENSO impacts on the wintertime anomalous Western North Pacific anticyclone to CO2 forcing. npj Clim. Atmos. Sci. 7, 299 (2024).

61. Zhang, W. et al. Ongoing intensification of anomalous Western North Pacific anticyclone during post-El Niño summer with achieved carbon neutrality. npj Clim. Atmos. Sci. 7, 317 (2024).

62. An, S.-I. et al. Asymmetric ENSO teleconnections in a symmetric CO2 concentration pathway. Environ. Res. Lett. 19, 124028 (2024).

63. Liu, C., An, S.-I., Yan, Z., Kim, S.-K. & Paik, S. Strong El Niño and La Niña precipitation—sea surface temperature sensitivity under a carbon removal scenario. Commun. Earth Environ. 5, 774, doi:10.1038/s43247-024-01958-8 (2024).

64. Eyring, V. et al. Overview of the Coupled Model Intercomparison Project Phase 6 (CMIP6) experimental design and organization. Geosci. Model Dev. 9, 1937-1958, doi:10.5194/gmd-9-1937-2016 (2016).

65. Piskala, V. & Huth, R. Asymmetry of day-to-day temperature changes and its causes. Theor. Appl. Climatol. 140, 683-690 (2020).

66. Zhang, J., Wu, L. & Dong, W. Land-atmosphere coupling and summer climate variability over East Asia. J. Geophys. Res.: Atmos. 116, doi:https://doi.org/10.1029/2010JD014714 (2011).

67. Betts, A. K., Ball, J. H., Beljaars, A. C. M., Miller, M. J. & Viterbo, P. A. The land surface-atmosphere interaction: A review based on observational and global modeling perspectives. J. Geophys. Res.: Atmos. 101, 7209-7225, doi:https://doi.org/10.1029/95JD02135 (1996).

68. Qiao, L. et al. Soil moisture–atmosphere coupling accelerates global warming. Nat. Commun. 14, 4908, doi:10.1038/s41467-023-40641-y (2023).

69. Samaniego, L. et al. Anthropogenic warming exacerbates European soil moisture droughts. Nat. Clim. Change 8, 421-426, doi:10.1038/s41558-018-0138-5 (2018).

70. Seneviratne, S. I. et al. Investigating soil moisture–climate interactions in a changing climate: A review. Earth Sci. Rev. 99, 125-161, doi:https://doi.org/10.1016/j.earscirev.2010.02.004 (2010).

71. Schneider, T., Bischoff, T. & Płotka, H. Physics of Changes in Synoptic Midlatitude Temperature Variability. J. Clim. 28, 2312-2331, doi:https://doi.org/10.1175/JCLI-D-14-00632.1 (2015).

72. Karl, T. R., Knight, R. W. & Plummer, N. Trends in high-frequency climate variability in the twentieth century. Nature 377, 217-220, doi:10.1038/377217a0 (1995).

73. Wu, F. T., Fu, C., Qian, Y., Gao, Y. & Wang, S. Y. High-frequency daily temperature variability in China and its relationship to large-scale circulation. Int. J. Climatol. 37, 570-582 (2017).

74. Gough, W. A. & Shi, B. Impact of coastalization on day-to-day temperature variability along China's East Coast. J. Coastal Res. 36, 451-456 (2020).

75. Wallace, J. M. & Hobbs, P. V. Atmospheric science: an introductory survey. Vol. 92 (Elsevier, 2006).

76. Liu, Q. A preliminary study on the climatological problems of interdiurnal temperature variability under global warming and their impacts on human health, Nanjing University, (2021).

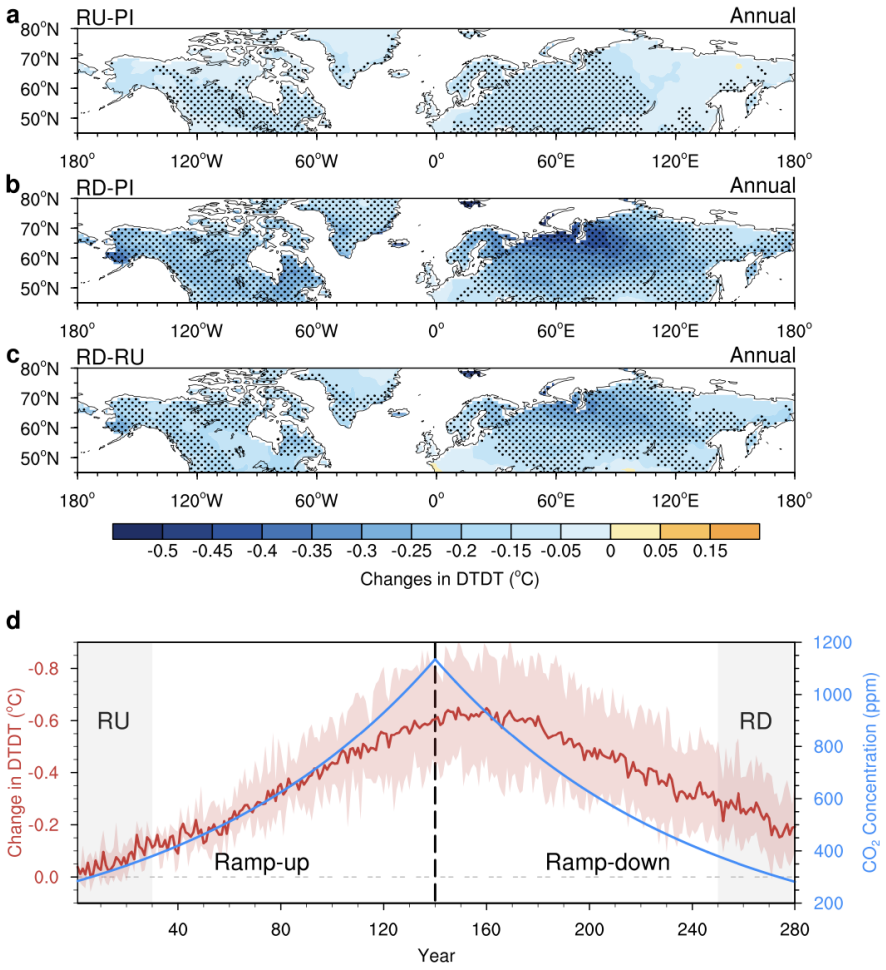

Fig. 1 | Annual response of day-to-day temperature variability (DTDT) to CO_2 forcing. a–b, Annual-mean DTDT anomalies during the RU **(a)** and RD **(b)** periods relative to the pre-industrial (PI) control. **c**, Difference in annual-mean DTDT between the RU (years 1–30) and RD (years 250–279) periods. Shading indicates changes in DTDT (°C). Black stippling in **a–c** marks regions where the multi-model mean (MME) change is statistically significant at the 90% confidence level based on a two-tailed Student's t-test, and where at least five of the six models agree on the sign of the MME change. **d,** Time series of atmospheric CO_2 concentration (blue line; ppm) and annual-mean DTDT anomalies (red line; °C) relative to the PI level over Northern Hemisphere mid–high latitudes (50°–75° N, 0°–360° E) in the idealized CO_2-removal experiments. The pink shading shows the inter-model spread, corresponding to the 25th–75th percentile range among the six models. The vertical dashed line denotes the CO_2 peak year (Year 140). Gray shading indicates the two 30-year periods with identical CO_2 concentrations: Years 1–30 (RU) and 250–279 (RD). In **d**, the left y-axis ranges from 0 to negative values.

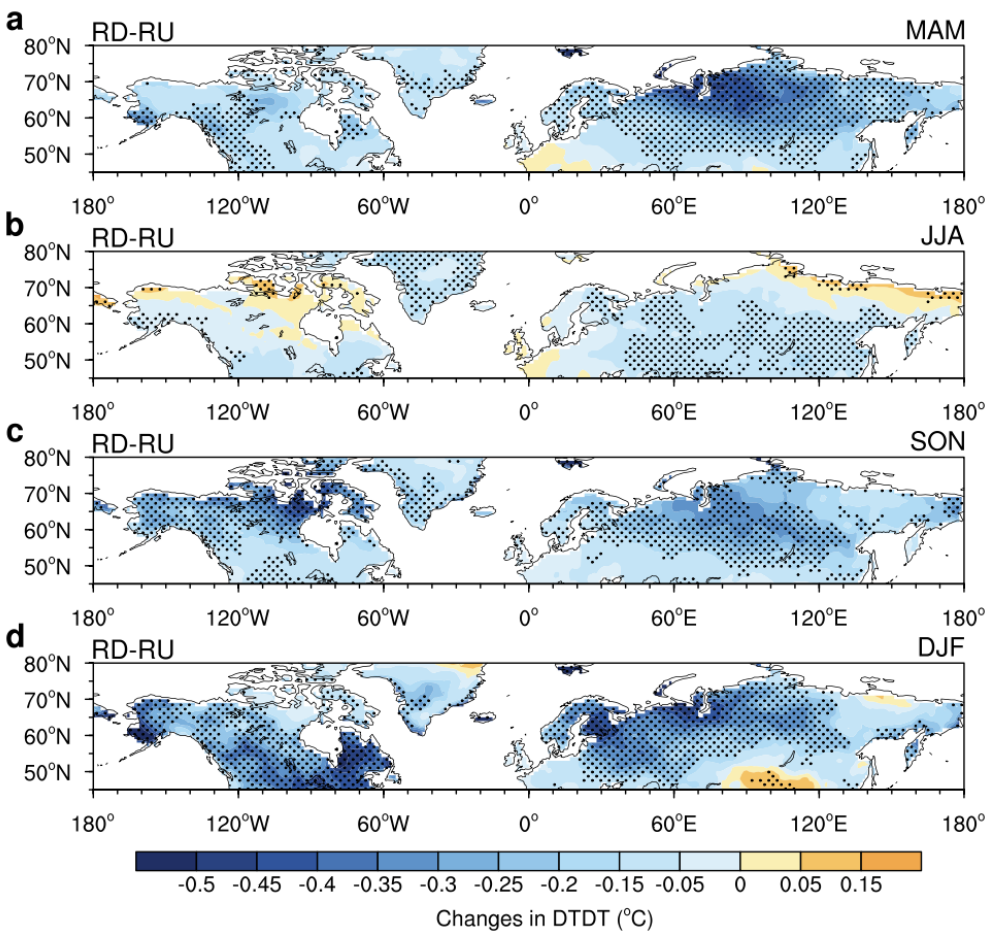

Fig. 2 | Seasonal response of DTDT to CO_2 forcing. a-d, MME differences in DTDT between the CO_2 ramp-up (RU; years 1–30) and ramp-down (RD; years 250–279) periods for (**a**) MAM, (**b**) JJA, (**c**) SON, and (**d**) DJF. Shading indicates the change in DTDT (°C). Stippling marks regions where the MME change is statistically significant at the 90% confidence level based on a two-tailed Student's t-test and where at least five of the six models agree on the sign of the MME change.

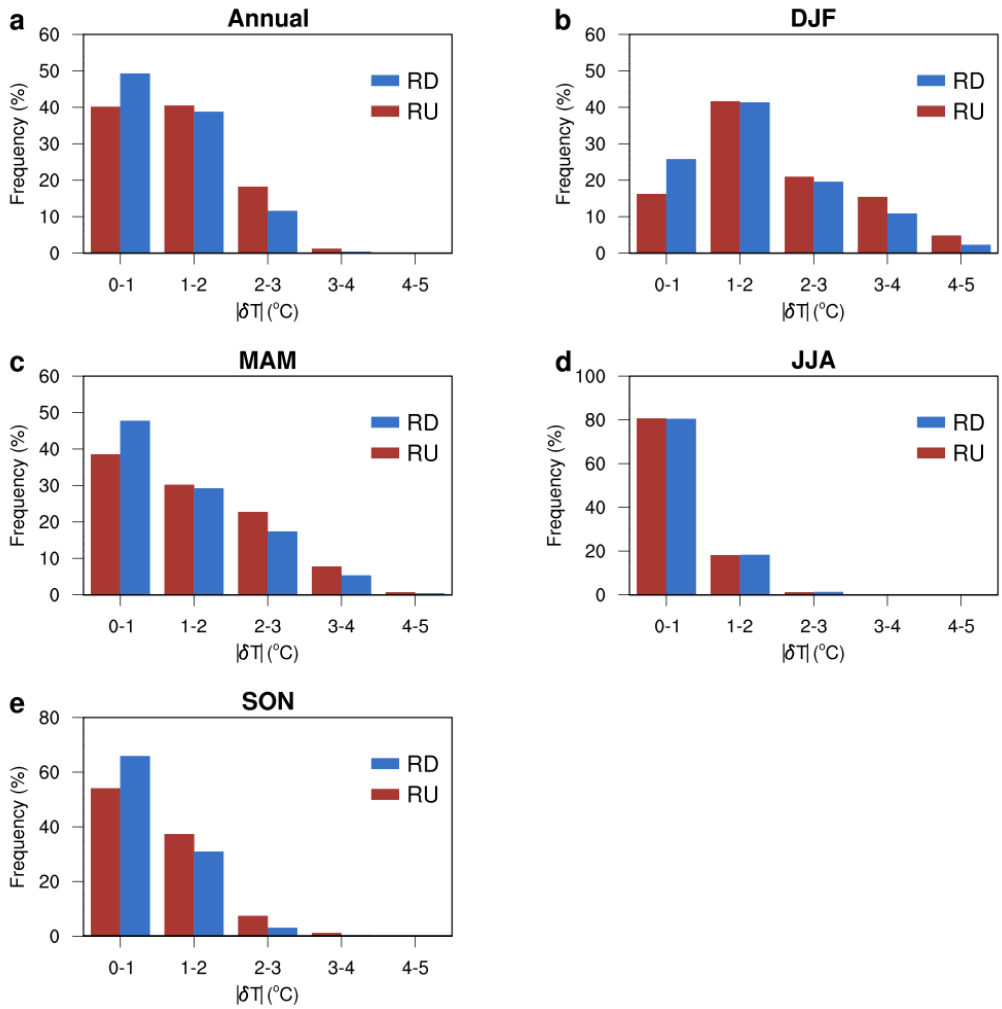

Fig. 3 | Distributions of day-to-day temperature differences during the CO_2 ramp-up (RU) and ramp-down (RD) periods. a, frequency distributions (%) of |δT| (°C) over Northern Hemisphere mid–high-latitude (50°–75° N, 0°–360° E) for the annual conditions during the CO_2 ramp-up (RU; years 1–30; red) and ramp-down (RD; years 250–279; blue) periods. **b–e,** Same as (**a**), but for individual seasons: (**b**) DJF, (**c**) MAM, (**d**) JJA and (**e**) SON. |δT| is defined at each grid cell as the absolute difference in daily-mean 2 m air temperature between two consecutive days and values are grouped into 1 °C bins.

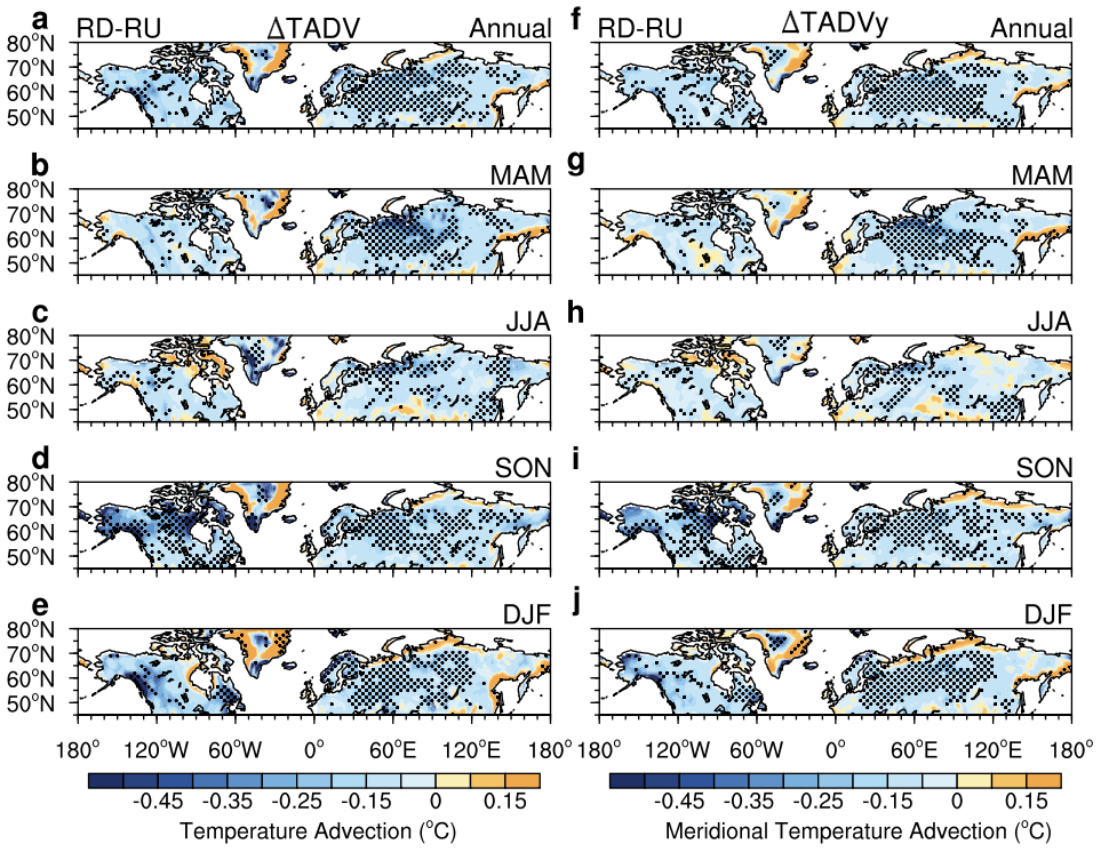

Fig. 4 | Changes in near-surface horizontal temperature advection and its key components between the CO_2 ramp-up and ramp-down periods. a–e, MME differences in near-surface horizontal temperature advection (ΔTADV) between the CO_2 ramp-up (RU; years 1–30) and ramp-down (RD; years 250–279) periods for the (**a**) annual mean, (**b**) MAM, (**c**) JJA, (**d**) SON, and (**e**) DJF. **f–j**, Same as **a–e**, but for near-surface meridional temperature advection (ΔTADVy). Shading indicates the MME response (°C) derived from the four-model ensemble (CanESM5, CNRM-ESM2-1, MIROC-ES2L, and GFDL-ESM4). Stippling marks regions where all four models agree on the sign of the MME change.

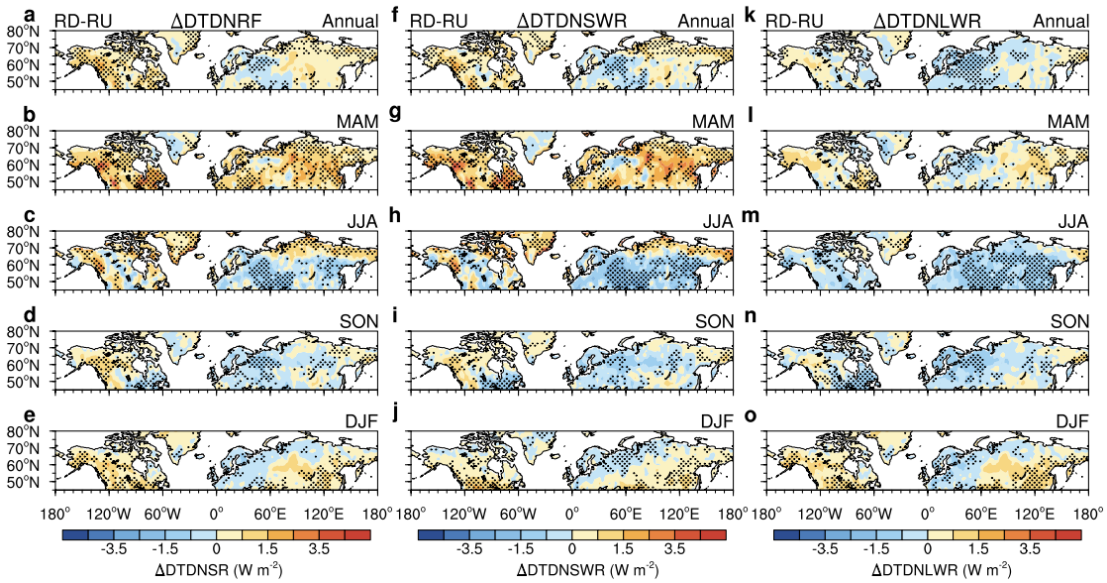

Fig. 5 | Changes in day-to-day variability of surface radiative fluxes between the CO_2 ramp-up and ramp-down periods. a–e, MME differences in the **day-to-day variability of surface net radiative forcing** (ΔDTDNRF) between the CO_2 ramp-up (RU; years 1–30) and ramp-down (RD; years 250–279) periods for the (**a**) annual mean, (**b**) MAM, (**c**) JJA, (**d**) SON, and (**e**) DJF. **f–j**, Same as **a–e**, but for the day-to-day variability of surface net shortwave radiation (ΔDTDNSWR). **k–o**, Same as **a–e**, but for the day-to-day variability of surface net longwave radiation (ΔDTDNLWR). Shading indicates the MME response (W m^{-2}) derived from the three-model ensemble (CanESM5, CNRM-ESM2-1, and MIROC-ES2L). Stippling marks regions where all three models agree on the sign of the ensemble-mean difference.